PHYSICAL REVIEW A VOLUME 44, NUMBER 11 1 DECEMBER 1991

Electron emission during interactions of multicharged N and Ar ions with Au(110) and Cu(001) surfaces

F. W. Meyer, S. H. Overbury, C. C. Havener, and P. A. Zeijlmans van Emmichoven
Oak Ridge National Laboratory, Oak Ridge, Tennessee 37831-6372

J. Burgdörfer
Oak Ridge National Laboratory, Oak Ridge, Tennessee 37831-6377
and Department of Physics, University of Tennessee, Knoxville, Tennessee 37996-1200

D. M. Zehner
Oak Ridge National Laboratory, Oak Ridge, Tennessee 37831-6057

(Received 15 July 1991)

We report measurements of energy distributions of electrons emitted during interactions 10q-keV N^{6+}, and Ar^{q+} ($q=7,8,9$) ions with Au(110) and Cu(001) surfaces at grazing angles. The electron energy distributions have been measured as a function of angle of incidence, observation angle, and target-crystal azimuth. For both Au and Cu targets, the projectile *KLL* Auger peak observed for the case of the N^{6+} projectiles is seen to consist of two components whose intensities have strikingly different dependences on incident perpendicular velocity. The main component of the *KLL* peak is attributed to subsurface electron emission and is modeled using a Monte Carlo simulation of the projectile trajectories in the bulk. The second component, observed only for the smallest incident perpendicular velocities, is attributed to above-surface *KLL* Auger electron emission and is modeled using computer simulations of the resonance neutralization-autoionization cascade that occurs prior to projectile penetration of the surface. In the case of the Au target, *NNV* and *NVV* transitions, attributed to vacancy transfer from the projectile *K* shell to the *N* shell of Au, are also observed. The Monte Carlo simulation of the subsurface contribution to the electron emission is able to reproduce the observed angle-of-incidence dependence of both the projectile and the target Auger electron intensities. In addition, it shows reasonable agreement with the observed dependences of the projectile *KLL* intensity on observation angle and crystal azimuth.

PACS number(s): 34.70.+e, 79.20.Nc, 79.90.+b

I. INTRODUCTION

Auger transitions that fill inner-shell vacancies in multicharged projectiles during interactions with metal surfaces have been studied by numerous investigators [1–7] in recent years. These studies have all found that, even for initially fully stripped or hydrogenlike incident projectiles, the energies of the observed Auger electrons correspond to Auger transitions in a projectile whose outer shells have already been almost completely neutralized. In addition, measurements [1,5] of the Doppler shifts observed as a function of observation angle showed that the inner-shell Auger transition occurs while the projectile is still on its initial trajectory, i.e., prior to appreciable projectile angular scattering in the bulk material. The apparent strong disagreement of the experimentally observed rapid neutralization of multicharged ions with the frequently invoked model of multicharged ion neutralization near surfaces proposed by Arifov *et al.* has been noted in a number of studies [5,6,8]. In this model, the primary neutralization mechanism is above-surface resonant multiple electron capture of metal conduction-band electrons into autoionizing projectile Rydberg levels. The subsequent complex autoionizing cascade requires time scales long compared to normal *K* Auger lifetimes, and thus cannot explain the almost complete neutralization of the projectile outer shells prior to *K* Auger decay.

In a recent paper [9] we have shown that this discrepancy can be resolved by considering the contribution due to electron emission below the surface. In the bulk, projectile neutralization by electron capture from loosely bound target valence-band levels directly to the projectile *M* and *L* shells can proceed on time scales significantly faster than those required for, e.g., *K* Auger decay. The depth in the bulk from which Auger electrons can be observed at their initial Auger transition energy is restricted to the first few crystalline layers of the target by the small electron inelastic mean free paths at the Auger transition energies in question. Using a Monte Carlo simulation of the detailed projectile trajectories inside the target material, we found that relatively little projectile angular scattering occurs over target depths comparable to the Auger electron inelastic mean free path. Therefore emission occurs while the projectile direction of travel is nearly the same as the incidence direction, in accord with the experimental Doppler shift observations. An analysis of the shapes of the observed projectile *K* Auger emission, together with theoretical fits of the Auger yields based on the above Monte Carlo simulation, indicated that below inverse projectile perpendicular velocities of about 100 a.u.$^{-1}$, subsurface electron emission is the dominant contribution to the observed *KLL* Auger peak. At larger inverse perpendicular velocities an additional, smaller component becomes discernible in the observed *KLL* peak. We ascribed this component to above-surface electron emission, and showed that its intensity had an angle of incidence dependence consistent with that expected for the resonance neutralization-autoionization cascade occurring above the surface.

In the present paper, we provide additional evidence supportive of this interpretation. After a description of the experimental approach and procedure, followed by a brief summary of our earlier electron spectra for 60-keV N^{6+} ions incident on Au(110) at 0.5°–20° grazing angles, in which both the projectile *KLL* and the Au target *NNV* and *NVV* Auger peaks will be discussed, we will present the results of more recent measurements of electron energy distributions for the same multicharged ion incident on Cu(001). We find significant differences in the intensities of the electron spectra observed for the two targets, which are also apparent for the case of incident Ar^{q+} ($q=7,8,9$) ions, results for which will also be presented. In addition to studying the variation with angle of incidence, we have investigated, for the case of the Cu target, the dependence of the electron spectra on observation angle, as well as on target-crystal azimuthal orientation. The above-noted target differences, as well as the measured variations with incidence angle, observation angle, and crystal azimuth are analyzed using our Monte Carlo simulation of the subsurface electron emission. It will be seen that this model can satisfactorily reproduce all the observed characteristics of the discrete features present in the measured electron spectra.

II. EXPERIMENTAL APPARATUS AND PROCEDURE

The experimental apparatus and technique have already been described elsewhere [2,9]. Briefly, a 10*q*-keV multicharged ion beam extracted from the ORNL ECR ion source was magnetically analyzed and then collimated by passage through two small apertures to give a 1-mm-diameter spot size on target at normal incidence, with an angular divergence of less than 0.2°. The targets used were clean Au(110) and Cu(001) single crystals mounted on an *x*-*y*-*z* manipulator located in an UHV chamber with a base pressure of 1×10^{-10} Torr. The target manipulator permitted independent crystal rotations about two axes, the first lying in the surface plane (used to select the ion beam angle of incidence) and a second normal to the crystal surface (used to select the azimuthal orientation of the crystal relative to the incident ion beam). The UHV scattering chamber was equipped with a CMA–electron-gun surface diagnostic system which was used to verify surface cleanliness, and an ion sputter gun. Surface sputter cleaning was performed using 1-keV Ar^{+} ions, and was routinely followed by a crystal annealing cycle to repair any surface damage caused by sputtering.

The electron spectra were measured using a compact electrostatic hemispherical sector analyzer (1.82 cm radius of curvature) mounted on a second manipulator (situated on a flange directly opposite to the target manipulator flange) which permitted proper alignment with respect to the beam spot on the target crystal and provided the capability of measuring ejected electron angular distributions. The analyzer was equipped with an einzel lens which could be used to increase the spectrometer acceptance angle (i.e., signal rate). The einzel lens could also be operated as a "zoom" lens to permit deceleration of the electrons prior to analysis, but was not used in that mode for the present set of measurements. The electron analyzer had a nominal energy resolution of 2.8% and was equipped with a multichannel plate particle detector (operated in pulse counting mode) whose front end was biased at +300 V to permit detection of even the lowest-energy electrons with good efficiency. A Helmholtz coil arrangement was used to cancel stray magnetic fields in the region of the target crystal. The electron spectrometer pass energy and data collection were controlled by a microcomputer-based data acquisition system configured as a multichannel scaler. The dwell time per channel was determined by target current integration to a preset accumulated charge.

The ion beam current intercepted by the second collimation aperture (see inset of Fig. 1) was used to normal-

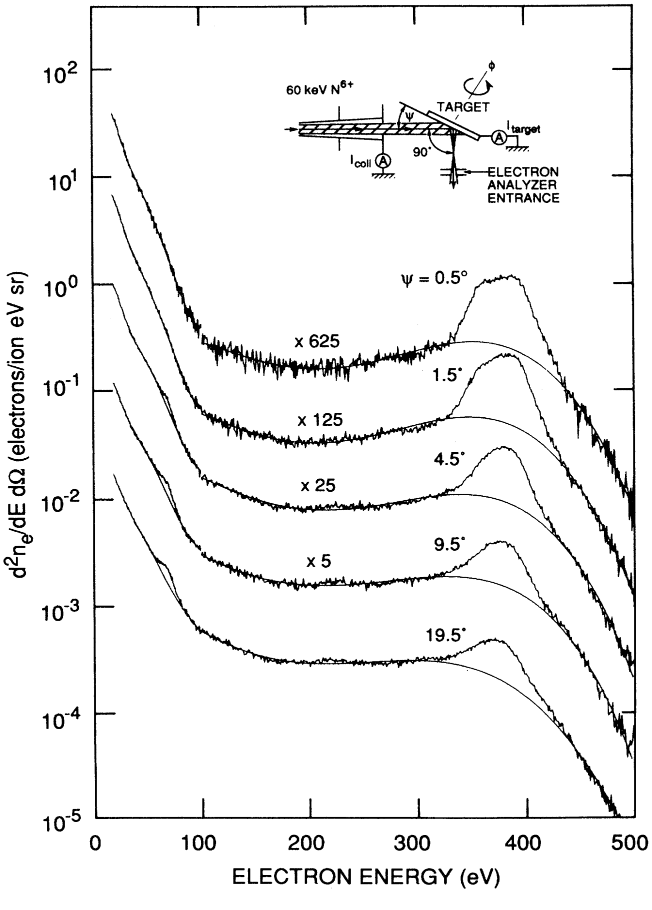

FIG. 1. Absolute experimental electron spectra observed for 60-keV N^{6+} ions incident on Au(110) at five different angles. The inset shows schematically the experimental configuration.

ize the measured electron spectra to the incident beam flux. The fraction of intercepted to transmitted beam current (current incident on the target crystal) was found to be almost completely independent of upstream tuning, in large part due to the placement of an additional, slightly larger aperture approximately 4.5 cm upstream of the final electron suppressed beam-collimation–monitoring aperture, which limited the intercepted beam to a thin annulus surrounding the transmitted beam. The calibration factor used to deduce beam flux incident on the target from beam intensity intercepted at this aperture was frequently monitored and found not to vary by more than 10% at a given beam energy.

The parameters required to put the measured double differential electron yields on an absolute scale were either determined experimentally, or determined from the known geometry and dimensions of our apparatus. On the basis of a compilation [10] of published studies, the channel plate electron detection efficiency was taken to be a constant 40% for the electron energy range 0–500 eV (which corresponds to 300–800-eV electrons striking the positively biased front of the channel plate). The diameter [full width at half maximum (FWHM)] of the electron spectrometer viewing region, determined by monitoring the measured electron count rate during spatial scans of the analyzer across a well localized source of electrons, was determined to be 2.75 mm when the einzel lens at the entrance to the analyzer was not used, and 3.27 mm when the einzel lens was optimized for maximum signal. For an extended line source of electrons (i.e., width much less and length much larger in spatial extent than the viewing region of the spectrometer) the einzel lens after optimization increased the signal count rate by a factor of 3.37. This factor represents a gain of solid angle of a factor of 2.84 in combination with the enhancement factor of 1.19 due to the increased size of the viewing region obtained by the use of the einzel lens.

For ion beam angles of incidence of less than about 15°, and electron detection normal to the surface, the length of target illuminated by the 1-mm-diam ion beam was greater than the target region viewed by the spectrometer, requiring the application of a well-defined geometric factor in the determination of the absolute electron intensity scale. For observation angles away from the surface normal, the geometric factor was also based on the projection of the illuminated target region onto a plane perpendicular to the spectrometer axis.

Care was taken to properly position the target crystal and the spectrometer with respect to the incident beam, as well as to optimize the Helmholtz coils. In order to assure longitudinal centering of the beam on the crystal target at grazing incidence angles, the crystal (with face parallel to the incident beam direction) was translated into the beam until the half intensity point on the beam current intercepted by the target was reached. At this position the 0° incidence angle setting of the manipulator rotation drive was checked by rotating the target slightly to either side of the nominal 0° setting and verifying a local minimum in intercepted beam current. The alignment of the analyzer with respect to the ion beam spot was performed by monitoring the intensity of high-energy (a few hundred eV) electrons ejected by the ion impact. With the ion beam incident at an angle close to perpendicular to the surface, making a small spot size and thus a very localized source of secondary electrons, and with the analyzer rotated to 90° relative to the incident beam direction, half intensity points were determined for translational scans of the analyzer parallel and transverse to the incident beam direction, respectively. The transverse and parallel positions of the analyzer were then set at the centers of the respective half intensity positions. After changing the analyzer observation angle by about 45°, the final translational degree of freedom of the analyzer was fixed by determining the half intensity points for scans in the vertical direction (i.e., towards and away from the ion beam). This procedure usually converged after two iterations. The analyzer and target thus having been physically aligned with respect to the incident ion beam by use of the high-energy electrons, the three orthogonal Helmholtz coils were adjusted iteratively by maximizing the intensity of low-energy (typically 5- or 10-eV) secondary electrons produced by the same incident ion beam. The Helmholtz coil adjustment using low-energy electrons was performed each time the angle of observation of the spectrometer was changed. The physical alignment of the analyzer using high-energy electrons was checked prior to each electron energy distribution measurement.

III. EXPERIMENTAL RESULTS

Using the approach outlined in the preceding section, we have measured electron energy distributions for N^{6+} and Ar^{q+} ($q=7$–9) ions incident on Au(110) and Cu(001) single crystals. Figure 1 shows electron spectra for 60-keV N^{6+} ions incident on Au in the range of incident angles 0.5–19.5°, all observed at 90° relative to the incident beam direction. The figure illustrates some general features shared by all the spectra to be presented in this paper. The measured electron spectra are dominated by a steeply falling continuum distribution which is strongly peaked at electron energies of a few eV. Superimposed on this continuum are discrete features that are identified either as target or projectile Auger transitions. For example, the peaks evident in Fig. 1 near 70 and 220 eV are $N_{6,7}VV$ and $N_{4,5}N_{6,7}V$ target Auger transitions, while the peaks centered near 380 eV are due to KLL Auger transitions in the N projectile. The projectile Auger peaks have associated energy straggling continua extending to lower energies, which are especially prominent when the projectile Auger transition occurs at sufficiently high energies that there is little overlap with the low-energy-peaked secondary electron continuum (see Fig. 1). This feature is better illustrated in Fig. 2, where the spectra for the different angles of incidence are superimposed on a linear intensity scale. The intensity of the straggling shoulder in relation to the Auger peak intensity is determined by the magnitude of inelastic electron energy loss in the bulk, and is therefore strongly influenced by the depth distribution over which the Auger electron emission takes place [11,12]. As will be discussed in greater detail in a later section of the paper,

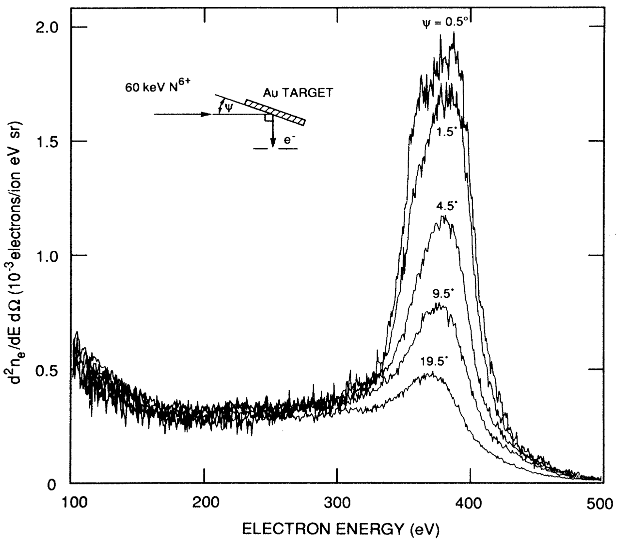

FIG. 2. Absolute projectile K Auger electron spectra for 60-keV N^{6+} ions incident on Au(110) at five different angles.

the depth distribution of the emitted projectile Auger electrons is a strong function of projectile incidence angle. It is mainly for this reason that the shoulders prominent in Fig. 2 do not scale with the K Auger peak intensities observed at the different incidence angles.

Figure 3 shows a comparison between electron spectra for 90-keV Ar^{9+} ions incident on Au and Cu targets at 10°, observed at an angle of 90° to the incident beam direction. It is noted that while the intensity of the continuum is greater by more than an order of magnitude for the Cu target in comparison to the Au target, the yield of projectile *LMM* Auger electrons, equal to the integrated intensity of the peak around 210 eV obtained after stripping off the continuum contribution (see solid lines in Fig. 3) is only about 50% larger than the corresponding yield for Au. Figure 4 shows electron spectra for different charge states of $10q$-keV Ar^{q+} ions ($7 \leq q \leq 9$) incident on Au and Cu at 10° and 1°. It is noted that for the case of the 1° incidence angle electron spectrum for Ar^{9+} incident on Cu, the total *LMM* Auger electron yield, integrated over 4π and assuming isotropic emission, is close to 1 e^{-}/ion, the maximum possible for one initial L-shell vacancy.

The variation of the electron spectra with observation angle (measured relative to the surface normal) is illustrated in Figs. 5 and 6 for 60-keV N^{6+} projectiles incident on Cu(001) at 1.6° and 20°, respectively. By a comparison of the two figures, it can be seen that the *KLL* peak area decreases more steeply as the observation angle is moved away from the surface normal for the 20° angle of incidence than for the more grazing 1.6° case.

In order to extract *KLL* Auger electron yields from the measured spectra, we developed two methods of background subtraction, illustrated by the two solid lines labeled A and B shown for each of the spectra in Fig. 5. The first method (curves labeled A) estimates the background by use of a sixth-order semilogarithmic polynomi-

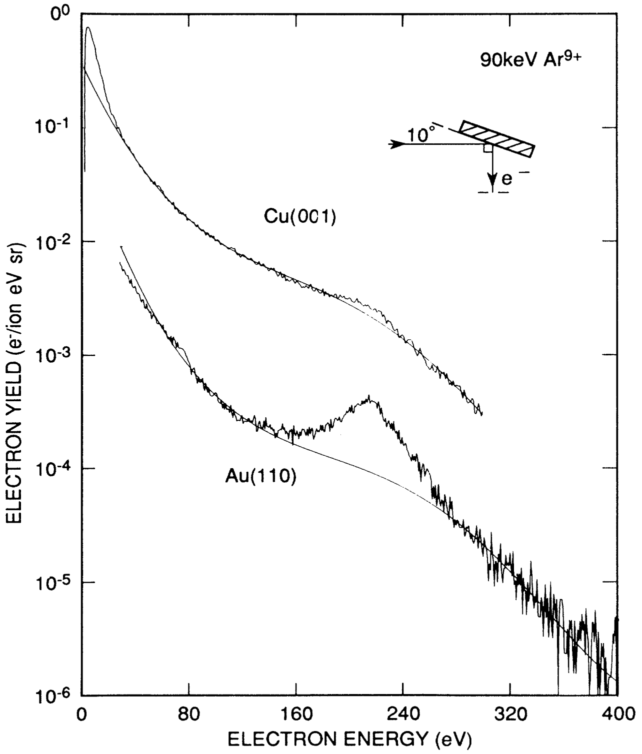

FIG. 3. Absolute experimental electron spectra observed for 90-keV Ar^{9+} ions incident on Cu(001) and Au(110) at 10°.

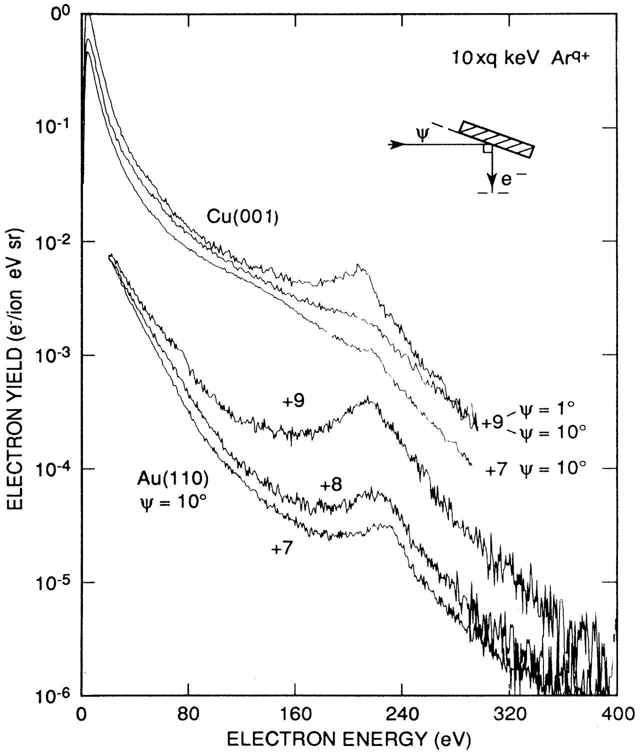

FIG. 4. Absolute electron spectra for $10q$-keV Ar^{q+} ions incident on Cu(001) and Au(110) at 1° and 10°.

al fit using as "windows" spectral regions on both sides of the peak dominated by continuum background. In the case of the projectile K Auger peaks, the "windows" were set immediately outside the range of possible K Auger transition energies for the entire manifold of possible charge states calculated using a Hartree-Fock atomic structure code [13]. For the N^{6+} projectiles this range was calculated to be 320–450 eV, which corresponds to the $1s2s^2$-$1s^2$ transition on the lower extreme and the series limit of the KLX transitions on the upper extreme, both for Li-like N. For observation angles other than 90°, this energy range was suitably Doppler shifted.

Implicit in the above method is the assumption that the peak and the underlying background have completely different origins, which is of questionable validity if the dominant projectile Auger emission originates from below the surface (as assumed in our working hypothesis). It is well known from solid-state Auger and photoemission studies that electron emission peaks originating in the bulk are accompanied by energy straggling continua on the low-energy side of the Auger peaks, which suggests the use of a background subtraction procedure such as suggested by Shirley [14] and later modified by Bishop [15]. This elegantly simple algorithm is based on the assumption that the "signal" at a particular energy E contributes a uniform background at all energies lower than E, and provides a good estimate of the background for the case of stationary Auger electron em-

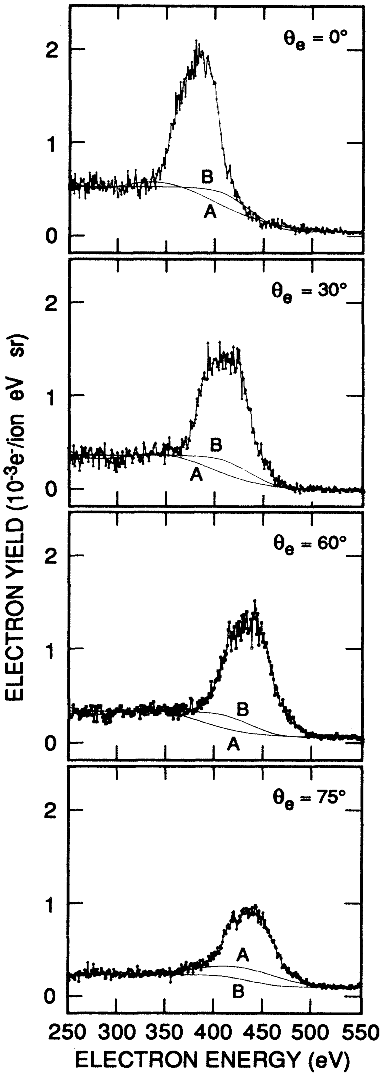

FIG. 5. Projectile K Auger electron spectra for 60-keV N^{6+} ions incident on Cu(001) at 1.6° as a function of forward observation angle (measured relative to the surface normal). Curves labeled A: background estimates obtained using polynomial fits; curves labeled B: background estimates based on applying modified Shirley method to extreme forward angle electron spectrum (see text).

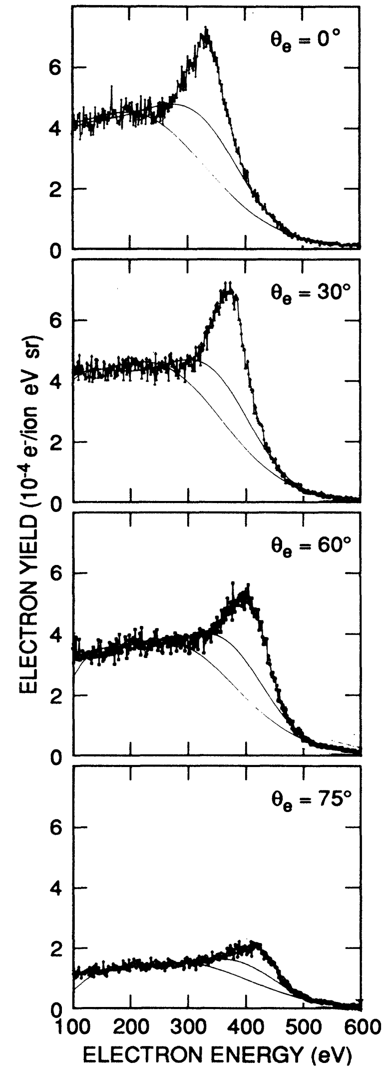

FIG. 6. Same as Fig. 5, except incidence angle is 20°. Both solid curves are polynomial fits obtained by using slightly different sampling "windows" (see text).

itters in the bulk, provided the Auger peak is well defined relative to the continuum tail on the low-energy side. However, for the case of moving emitters the situation is complicated by the fact that Auger electrons of rest frame energy E can contribute to background at energies larger than E, if, for example, they are emitted in the forward direction and then elastically scattered in the bulk toward the spectrometer. This effect is minimized, however, when the spectrometer is situated at the extreme forward angles. The second method employed for background stripping of the projectile peaks in our electron spectra entailed application of the modified Shirley method to a spectrum measured at such a forward observation angle (e.g., the $\theta_e = 75°$ spectrum of Fig. 5), and then using the resulting background shape at other angles as well, by scaling to match the low-energy continuum shoulders at each observation angle. This is the procedure used to obtain the curves labeled B in Fig. 5. For grazing angles of incidence, and for observation angles close to the surface normal, the two background estimation methods give projectile peak areas that agree to within about 15%.

When extreme forward observation angle spectra were not available, the polynomial fits were used as an approximation to the modified Shirley method. The first method was also used in cases when the extreme forward angle spectra were available, but the projectile Auger peak was no longer clearly defined relative to the low-energy shoulder. Such is the case for the 20° incident angle spectrum shown in Fig. 6. The lower solid line shown in that figure is a polynomial fit obtained using the "windows" described above, while the upper line shows the effect of an arbitrary narrowing of the fit "windows." The difference between the two fits is the dominant source of uncertainty in the projectile Auger peak areas at the largest incidence angles.

To conclude this section on the measured electron spectra, we show in Fig. 7 typical electron energy distributions observed normal to the surface, for two different crystal azimuthal orientations relative to the incident beam direction. The azimuthal rotation is measured relative to the [100] direction (i.e., $\phi = 0°$ corresponding to the [100] direction). The spectra were obtained with 60-keV N^{6+} ions incident on Cu(001) at 5° along the [110] azimuth ($\phi = 45°$) and along $\phi = 35°$. In comparing the two spectra it is seen that the KLL peak is slightly, yet significantly smaller off the [110] direction than it is for incidence along the [110] azimuth. We find similar azimuthal variations for the other angles of incidence as discussed in Sec. VII.

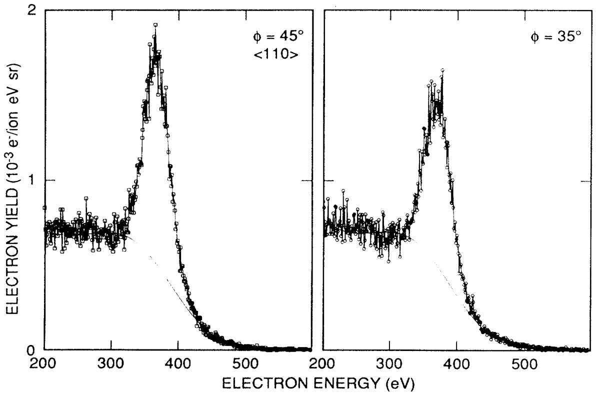

FIG. 7. Electron spectra measured for 60-keV N^{6+} ions incident on Cu(001) at 5° along two different azimuths; the observation direction is normal to the surface.

IV. MONTE CARLO SIMULATION

We have recently suggested [9] that many of the discrete features in low-energy, multicharged ion-induced electron spectra observed during interactions with surfaces could be explained by assuming that most of the electron emission occurs after the projectile has penetrated the surface of the metal target material. This conclusion was based on extensive calculations of the projectile trajectories inside the solid target using the MARLOWE Monte Carlo simulation code [16]. We developed a model in which the neutralization and deexcitation of the projectile was assumed to progress in three sequential stages. In the initial stage (projectile population fraction P_1) the projectile carries a K vacancy and has an empty L shell; in the intermediate stage (fraction P_2) the K vacancy still survives, but the L shell has become (nearly) filled; in the final stage (fraction P_3) the K vacancy has been filled. This three-component system is described by the following set of coupled differential equations:

$$\frac{dP_1}{dt} = -R_L P_1 - p_K \frac{d\Theta}{dt} P_1 , \tag{1a}$$

$$\frac{dP_2}{dt} = R_L P_1 - R_K P_2 - p_K \frac{d\Theta}{dt} P_2 , \tag{1b}$$

$$\frac{dP_3}{dt} = R_K P_2 + p_K \frac{d\Theta}{dt} (P_1 + P_2) , \tag{1c}$$

$$P_1 + P_2 + P_3 = 1 \tag{1d}$$

where R_L is the rate of L-shell filling, and R_K is K Auger decay rate. The last terms in Eqs. (1a) and (1b) represent K-vacancy transfer from the projectile, which was incorporated to permit calculation of target Auger electron production. The step function Θ is dependent on the history of the trajectory, and increases its value in unit steps each time a collision occurs having a distance of closest approach less than d_{crit}. For such collisions K-vacancy transfer is assumed to occur with probability p_K. The time evolution of this system is determined by numerical integration along the calculated projectile trajectories inside the bulk. A screened Coulomb ion-solid interaction potential suggested by Ziegler, Biersack, and Littmark [17] is used. The simulation is started at 3 a.u. above the surface plane.

Using MARLOWE, sets of trajectories were generated and followed in detail [18]. For each time interval between collisions with target atoms, the incremental projectile K Auger yield is calculated. At each collision with apsis less than d_{crit}, the target Auger yield is incremented. The *observed* projectile and target electron yields at a given observation angle θ_e were calculated by weighting the respective incremental yields by the probability for electron escape from the metal without inelastic scattering in the direction of observation, given by $(1/4\pi)\exp[-z/(\lambda\cos\theta_e)]$. The variable z is the depth below the surface, θ_e the angle of observation relative to the surface normal, and λ the electron inelastic mean free path. No kinetic energy change or refraction effects of the emitted electron were assumed as a result of the work-function-related potential step at the surface, due to the magnitude of the projectile Auger electron energies of interest (> 320 eV). Isotropic emission in the laboratory frame is assumed. Doppler broadening effects due to angular scattering and straggling of the projectiles in the bulk prior to K Auger electron emission were accounted for by employing the local projectile velocity vector in the transformation required to obtain the laboratory frame energies of the electrons emitted by the projectile. Gaussian-shaped emitter-frame K Auger electron distributions with selected peak energies and widths were used to fit the corresponding observed (i.e., laboratory frame) electron distributions. Typically 1000 trajectories were calculated for each set of initial conditions, which gave yields which were statistically accurate to within a few percent.

The L-shell filling rate R_L was determined by fitting the Monte Carlo results for the projectile Auger yields to the experimental data for each target. For a given projectile energy, R_L was assumed to be a function only of the target material, i.e., it was assumed to be *independent* of incidence angle, crystal azimuth, and observation direction. The value of the electron inelastic mean free path of 10 Å used both in the Au and Cu target simulations for the ~380-eV projectile Auger electron was taken from the literature [19]. The projectile K Auger decay rate R_K was taken to be $1\times10^{14}\text{s}^{-1}$, a value very close to the tabulated [20] rate for neutral nitrogen.

Figure 8 shows, for both Au and Cu targets, the dependence of the calculated projectile Auger electron yields on the L-shell filling rate, R_L for one particular azimuthal orientation. Similar curves were generated for other possible azimuths and assumptions of surface damage. On the basis of the entire family of curves, a value of R_L was chosen to give the best agreement of the calculated and measured K Auger electron yields over the whole range of incidence angles investigated. Values of 1×10^{14} and $5\times10^{14}\text{s}^{-1}$ were found for Au and Cu, respectively [21]. Since the observed yield of *target* Auger electrons resulting from K-vacancy transfer is low in comparison with the observed projectile K Auger yields, d_{crit} and p_K could be adjusted independently of R_L in order to fit the measured dependence on incidence angle without significantly affecting the calculated projectile electron yields. Having determined appropriate model parameters, it is possible to determine the dependence of the observed projectile and target Auger spectra on projectile angle of incidence, laboratory observation angle, azimuthal orientation, and crystal perfection as discussed below.

The description of the projectile L-shell filling in terms of a continuous, macroscopic rate, R_L, instead of discrete, binary collision events with target atoms, is a simplifying, yet physically reasonable, approximation that is based on the assumption that the predominant L-shell filling mechanism is (multiple) electron capture from only semi-localized valence-band levels of the metal target (i.e., the $3d^{10}$ or $5d^{10}$ bands in the case of Cu and Au targets, respectively). Initially, capture is most likely into the M shell of the projectile and, in later neutralization stages, directly into the L shell. The rapid LMM Auger decay that follows multiple electron capture into the M shell is assumed to be contained in R_L, and defines an upper bound to the L-shell filling rate in the early stages of neutralization. A further *a posteriori* justification of using a continuous neutralization rate is the fact that, for the investigated projectile energies, the number of binary collisions encountered in the MARLOWE simulations was always large (i.e., always greater than 20, and more typically greater than 100), irrespective of the initial conditions specified (such as target properties, incidence angle, or crystal azimuth).

The extent to which core target levels participate in the projectile neutralization is most likely small. Substantial binding energy shifts of the initially empty projectile L

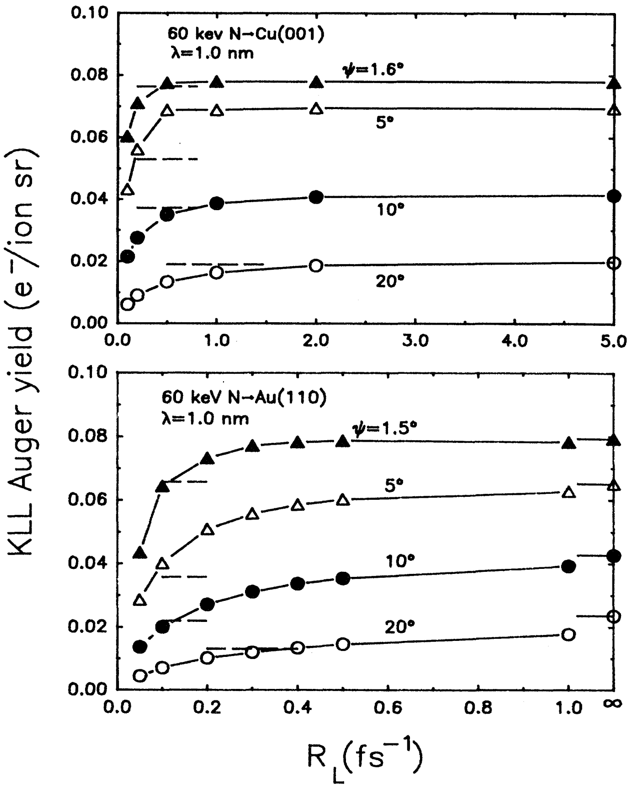

FIG. 8. Calculated projectile K Auger yields for 60-keV N^{6+} ions incident on Au(110) and Cu(001) at different angles as a function of the assumed neutralization rate R_L. The horizontal dashed lines represent the experimental yields determined at each incidence angle.

and *M* shells are likely because of the significant screening of the projectile charge resulting from the large "free" electron concentration inside the target bulk. This screening has the additional effect of restricting the number of bound excited states possible inside the bulk. Recent [22] linear-response-theory calculations of the bound excited state spectrum of a hydrogenic ion of charge *q* in the presence of a dynamical screening potential indicate that for electron densities appropriate for Cu and Au, the *M* shell is the highest bound excited level of N^{6+} at the velocities relevant to the present experiment. A similar conclusion was reached by earlier treatments [23,24] assuming a static screened Coulomb potential. On the basis of these calculations, direct capture to the *M* shell may be possible in the initial stages of projectile neutralization. However, as has been pointed out in Ref. [22], the collisional broadening of only weakly bound levels can be significant. Such broadening would, of course, need to be considered in calculating the appropriate energies and line shapes of the subsequent *LMM* Auger transitions by which the *M*-shell electron population is depleted. As regards the total number of bound electrons possible on a slow *N* projectile traversing a metallic solid, calculations [25] using a density-functional approach show that the 2*p* projectile electrons form a resonant state embedded in the metal conduction band, implying that the *M* shell is most likely unbound in the final stages of neutralization. For these projectiles, the calculations give an effective charge (defined in terms of its stopping power compared to that for equivelocity protons) of about 1.5 at the screening lengths appropriate for Cu and Au. The similarities [26] between *KLL* transitions of second row elements observed *at rest* in solids and *in vacuo* suggest the possibility that the increased binding of the outer electrons in the presence of a *K* vacancy causes the 2*p* shell to drop energetically below the bottom of the conduction band, and thus to assume a more atomic character. It is unlikely, though that the *M* shell is similarly affected, due to its significantly larger mean radius. Confirmation of this speculation will have to await density-functional calculations of bound excited states of ions in the presence of a static or dynamic screening potential, which have not been performed to date [27]. This possible evolution of the *M* shell from an initially bound to an unbound one toward the end of the neutralization process may explain the "missing" *LMM* Auger intensity that has been noted [5,6] in the comparison of projectile *K* Auger and *L* Auger electron yields. As was noted already in connection with the *LMM* Auger line shapes, theoretical evaluation of the *KLL* line shapes for *moving* emitters in solids will also require incorporation of collisional broadening effects, which most likely will be significant for second row elements.

V. ANGLE OF INCIDENCE DEPENDENCE

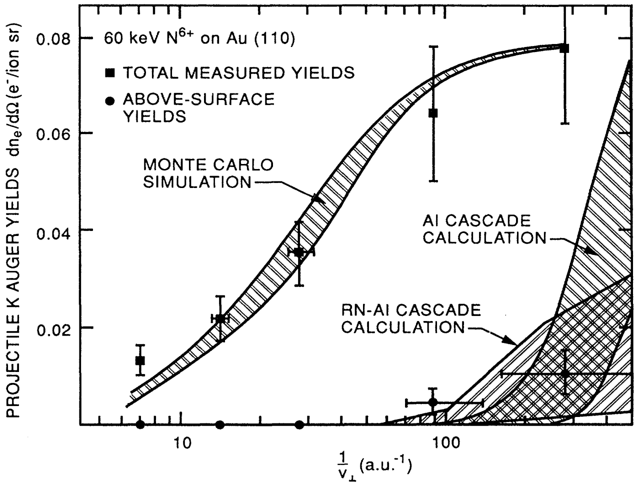

FIG. 9. Measured total and above-surface *K* Auger electron yields, $dn_e/d(\Omega)$, observed normal to the incident beam direction for 60-keV N^{6+} ions incident on Au(110), as a function of inverse perpendicular projectile velocity. Also shown are Monte Carlo simulation results for the subsurface *K* Auger components, as well as two different calculations of the above-surface neutralization components. Band labeled AI cascade is calculation from Ref. 9; band labeled RN-AI cascade is more rigorous treatment from Ref. [32] that includes the effects of image potential acceleration on the projectile trajectories.

Figures 9 and 10 summarize the differential projectile *K* Auger electron yields for the Au(110) and Cu(001) targets observed at 90° to the incident beam direction, obtained by integration of the *K* Auger peaks remaining after background subtraction. Yields are shown as a function of $1/v_\perp$, which for fixed incident energy is directly related to incidence angle. For both targets, the yields approach at the very smallest angles of incidence a value that corresponds to a total (angle integrated) yield of one electron per incident ion, if isotropic electron emission is assumed. This is the maximum yield possible for an incident ion with one initial *K*-shell vacancy. The Monte Carlo simulation results for these two targets are

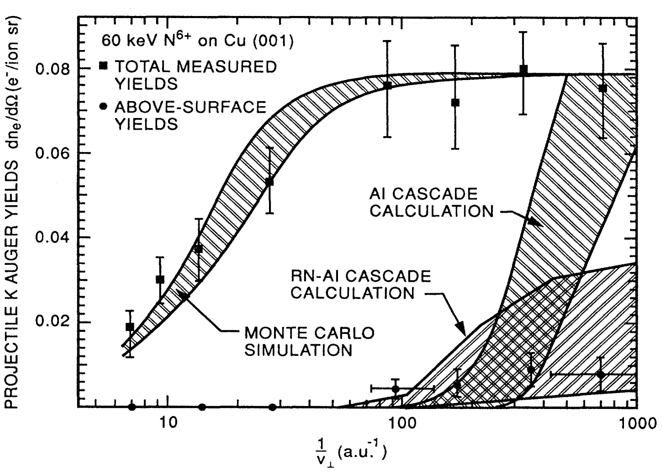

FIG. 10. Same as Fig. 9, but for a Cu(001) target.

also displayed in the two figures. In the case of the Cu(001) target, the simulation results showed significant variations with the azimuthal target orientation within the 5° uncertainty range of the mechanical azimuth setting. The band delimiting the simulation results for Cu(001) in Fig. 10 represents the variation in Auger yields obtained in the range of azimuthal angles within 5° of the nominal [110] crystal orientation for which the measurements were made. In the case of the Au(110) target, the crystal azimuth was unknown. In addition, the Au crystal was insufficiently annealed subsequent to sputter cleaning, as a result of which there was probably a significant degree of surface damage present during the Auger electron yield measurements. The band delimiting the simulation results for Au(110) in Fig. 9 represents the variation of yields obtained over a broad range of crystal azimuths, and for various site-vacancy fractions in the first two crystal layers to simulate the actual surface damage.

As can be seen from the two figures, the simulation results reproduce the measured yield dependences on incidence angle quite well. For both targets, the simulation systematically underestimates the observed yields at the largest incidence angles ($1/v_\perp < 10$). The background stripping procedure used has the largest uncertainty for these angles, and may underestimate the "true" background for these cases. Also, the applicability of the simplified electron transport treatment used in the simulation may become questionable at the largest angles of incidence investigated.

The significant difference between the L-shell filling rates giving the "best fits" for the two targets, i.e., 1×10^{14} and $5\times10^{14}\mathrm{s}^{-1}$ for Au and Cu, respectively, was somewhat surprising. Part of the difference is accounted for by the difference in target densities [28] (5.9×10^{22} for Au versus $8.45\times10^{22}\mathrm{cm}^{-3}$ for Cu), since (at least for amorphous targets) the rate can be written as $R_L = nv\sigma$, where n is the target density, v the projectile velocity, and σ an effective L-shell neutralization cross section. It should be noted, however, the two R_L's were deduced under the assumption that the two targets are characterized by identical values (i.e., 10 Å) of the electron inelastic mean free path for ~380-eV electrons. While this assumption finds support in the literature, more recent studies [29] suggest a stronger Z dependence (finding for 250-eV electrons $\lambda = 7.3$ Å for Ni and 5.3 Å for Pt). Using in the case of Au a λ for 380-eV electrons smaller by the same factor as the above numbers for Pt/Ni results in an increase in R_L of a factor of 2, i.e., R_L would become $2\times10^{14}\mathrm{s}^{-1}$. That would leave the effective neutralization cross section for Cu only about 1.75 times that for Au. This difference might be explainable in terms of the different valence-band density of states [30] and core level energies for the two targets.

A crucial question that still needs to be addressed in order to validate our interpretation in terms of subsurface electron emission is the effect of projectile angular scattering and particle reflection on the simulated K Auger electron spectra. If significant projectile angular scattering were to occur prior to K Auger decay within the first few layers of the surface, then the observed electron emission would be Doppler broadened considerably, and, furthermore, would not display Doppler shifts as a function of observation angle consistent with emission along the initial ion trajectory, as has been noted experimentally. Figure 11 shows simulated K Auger electron spectra for both Au and Cu targets as a function of incidence angle. In order to obtain spectral shapes in reasonable agreement with the observed ones, a Gaussian projectile-frame Auger electron distribution was assumed, peaked at 380 eV and having a 50-eV FWHM. This "source function," arbitrarily scaled, is shown as the dashed curve superimposed on the simulated electron spectra for 5° incidence angle. In addition, an experimental spectrum for 20° incidence angle is shown for Cu. As noted above, at this angle of incidence the poorest agreement between the simulation results and measured *yields* was found. Even for this angle, however, the simulated and measured *shapes* are in reasonable accord. To permit additional comparison, Fig. 12 shows experimental background stripped K Auger spectra for different angles of incidence on Au (the spectra for Cu look qualitatively similar). Given the uncertainty in background determination, the agreement in spectral shapes is satisfactory at all angles. Moreover, in view of the small difference between the Gaussian "source function" and simulated spectra evident in Fig. 11, it can be concluded that the effects of angular scattering and particle reflection are relatively subtle, and in particular do not result in significant shifts of the peak energies of the simulated spectra.

We conclude the discussion of the angle-of-incidence dependence of the Auger electron spectra by considering the dependence of the target Auger spectra observed in the case of the Au target. The inset of Fig. 12 shows the variation with incidence angle of the 69-eV $N_{6,7}VV$ target peak. Although not obvious from the inset, the intensity of the 69-eV peak is maximum in the range of angles 5–10°, falling off slightly towards larger angles and quite steeply towards smaller angles. The 220-eV $N_{4,5}N_{6,7}V$ Au peak is roughly a factor of 10 smaller in intensity that the 69-eV peak, and displays an even more pronounced intensity maximum in the angular range 5°–10°. As has

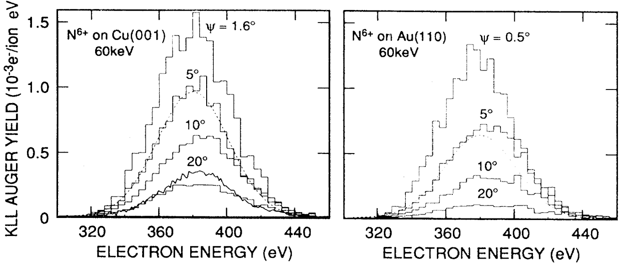

FIG. 11. Comparison of the Monte Carlo simulation results for the K Auger line shapes obtained for 60-keV N^{6+} ions incident on Cu and Au targets at different incidence angles. Superimposed on the 5° incidence angle results is the assumed Gaussian source function, arbitrarily scaled. Also shown on the same absolute scale is the experimental electron spectrum observed for 20° incidence angle on Cu(001).

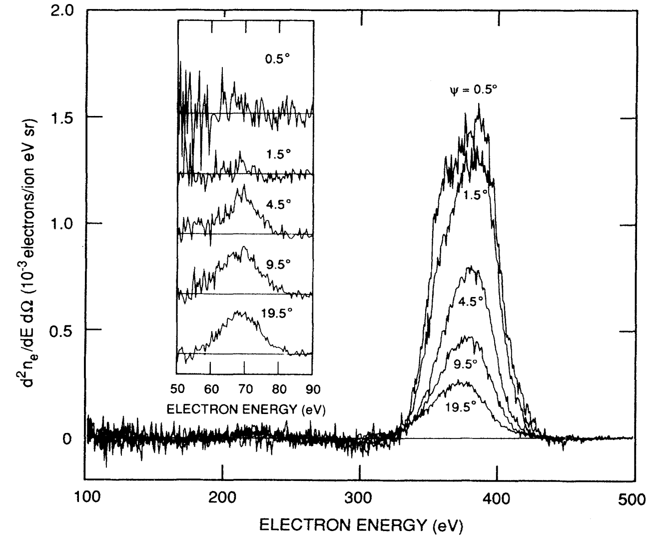

FIG. 12. Background stripped projectile K Auger and target NVV peaks (inset) observed for 60-keV N^{6+} ions incident on Au for various incidence angles.

been noted above, we have modeled the production of the $N_{4,5}$ Au target vacancy by an inner-shell [31] electron capture process to the projectile K shell, defined in terms of a critical impact parameter within which the capture probability is nonzero. The binding energy of the $N_{6,7}$ vacancy, relevant to production of the 69-eV peak, is sufficiently small that we cannot exclude other processes which do not involve the projectile K shell (i.e., not accounted for in our simulation) as being possible in its formation. In Fig. 13 we show the simulation results for the observed 220-eV Au Auger electron yields, obtained by assuming a critical distance d_{crit} of 0.4 Å and capture probabilities p_K in the range 0.007–0.016 which depended on the various assumptions made about details of the Au target (see caption of Fig. 13). As can be seen, the simulation reproduces the experimentally observed variation with incidence angle reasonably well. Also shown in the figure are simulation results for total (i.e., unweighted by escape probability) target and projectile Auger electron production. Comparison of the total and observed yields illustrates the fact that the increase in observed target Auger yield for $1/v_\perp < 30$ is due to an increase in Auger electron escape probability as the projectile trajectories (along which the target Auger electrons are "born") lie progressively closer to the surface as the incidence angle is decreased. This effect is also responsible for the increase of the observed projectile K Auger yield with decreasing angle. The reason for the precipitous decrease in the observed target yields at the smaller incidence angles is primarily due to a progressive shift to larger distances of the apsis (distance of closest approach) distribution characterizing the close encounters between projectiles and target atoms. As a result, progressively fewer of the binary collisions are sufficiently close for vacancy transfer to occur. Especially at the grazing angles, the apsis distribution was found to depend quite sensitively on the chosen target parameters, e.g., single crystal versus amorphous, crystal azimuth orientation, and the degree of surface damage assumed in the simulation. As a result, the simulation results for the observed target yields also depended quite strongly on the target specification in this range of angles, as is illustrated in the figure.

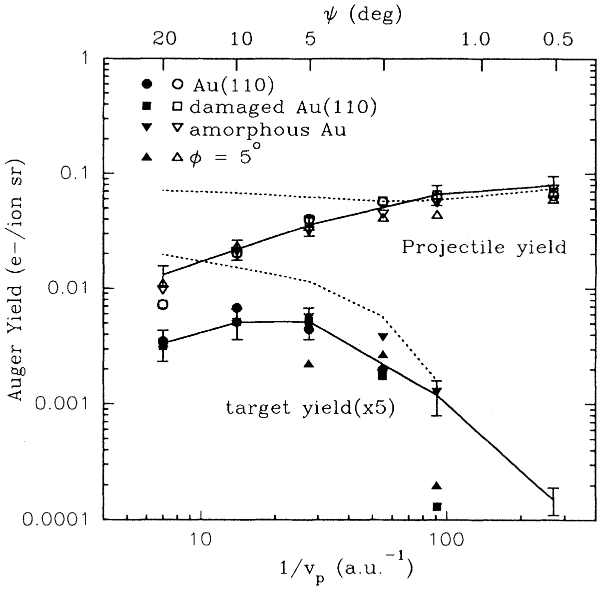

FIG. 13 Monte Carlo simulation results for observed projectile K Auger (open symbols) and Au target NNV (solid symbols) electron yields for different target specifications, compared to the experimental measurements (denoted by vertical error bars). For the simulated NNV electron yields, d_{crit} was assumed to be 0.4 Å, and p_K was taken to be 0.016 for the 0° azimuth (●) and surface-damaged (■) targets, 0.009 for the amorphous target (▼), and 0.007 for the 5° azimuth case (▲). Simulation results for the total projectile and target NNV Auger electron production are shown as dashed lines, illustrating the attenuation effects at the various angles due to the varying projectile penetration depths. The total electron production simulations were made assuming amorphous Au.

VI. OBSERVATION ANGLE DEPENDENCE

Figure 14 summarizes the measured and simulated observation angle dependence of the projectile K Auger electron yields for 60-keV N^{6+} ions incident along the [110] direction of Cu(001) at two different angles of incidence. For the 1.6° incidence angle, reasonable agreement is obtained between the simulation and the experimental results out to observation angles of 60°. At 75° the measured result lies significantly below the simulation. Determination of the spectrometer viewing region correction is difficult for this combination of grazing incidence and observation angles along the [110] crystal azimuth, since this direction is at 45° to the edges of the rectangularly shaped crystal. At 1.6° incidence angle and 75° observation angle, the beam overfills the crystal target, and

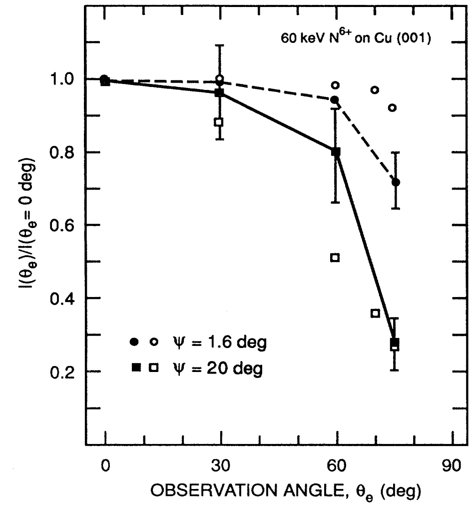

FIG. 14. Comparison of the experimental (solid symbols) and simulated (open symbols) forward observations angle distribution of the projectile K Auger electron emission (θ_e is measured relative to the surface normal). The solid and dashed lines are drawn through the measured data points to guide the eye.

the spectrometer views a region of space that is larger than the crystal diagonal illuminated by the ion beam, whose length varies depending on the location of the ion beam impact relative to the center of the target crystals. The actual illuminated target length will be overestimated if the beam and crystal centers were not coincident, resulting in an underestimation of the measured electron yields. For the case of the 20° incidence angle spectra, the spectrometer viewing region exceeded the size of the target region illuminated by the beam at all observation angles, eliminating the above uncertainty in the viewing region correction. The difference in measured and simulated observation angle dependences for this incidence angle arises at least in part from the difficulty of determining the proper background to be stripped at each observation angle. Unlike the 1.6° incidence angle, we could not use the modified Shirley method described in a previous section for the background determination. However, the polynomial fits used instead would, if anything, tend to overestimate the backgrounds away from normal observation angles, and so do not appear to be the cause for the experimentally determined yields lying above the simulation results at intermediate observation angles.

Despite these disagreements with the simulations in the details of the angular distributions, the measurements do reproduce the general trends expected for subsurface electron emission that are evident from the simulations. First, for both incidence angles, the electron yields decrease toward grazing observation angles, and second, this decrease is more pronounced at the steeper incidence angle of 20°. The first effect is due to the increased distance the Auger electrons have to travel in the bulk in order to escape in the observation direction, while the second results from the increase in the mean depth from which the Auger electrons originate as the incidence angle is increased. It is noted that de Zwart [1] has observed a similar evolution of the Auger electron angular distribution with decreasing incident perpendicular velocity.

VII. AZIMUTHAL ORIENTATION DEPENDENCE

As has been previously noted, for some of the incidence angles the simulation results showed significant sensitivity to the crystal azimuthal orientation with respect to the incident beam direction. Figure 15 shows the simulation results for 60-keV N^{6+} projectiles incident on Cu(001) at four different incidence angles, together with the measured yields. The electron emission is in the direction of the surface normal. As might be expected, the simulation shows relatively little azimuth dependence for the most grazing angle, 1.6°, since the very shallow ion trajectories in this case sample only the top one or at most two crystal layers. For the 5° and 10° angles of incidence, however, statistically significant variations (of the order of 10–30 %) are found in the simulated K Auger yields. The statistical uncertainties of the simula-

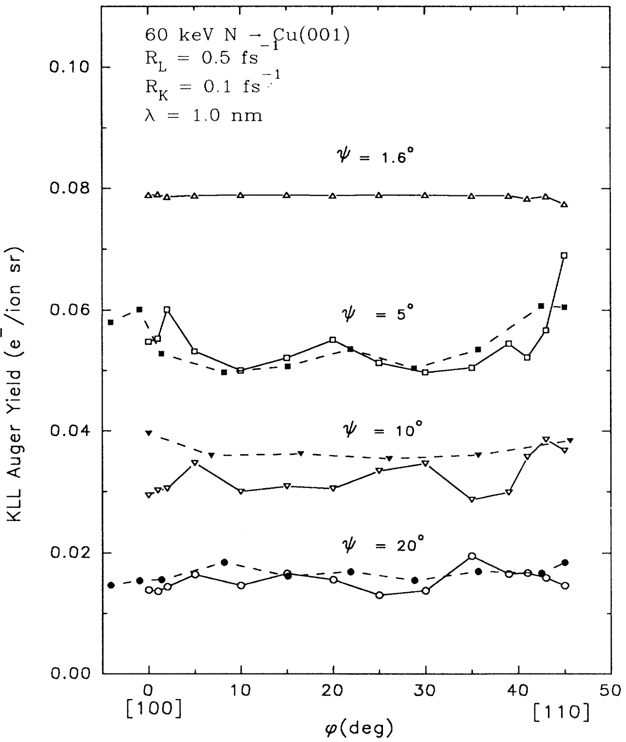

FIG. 15. Comparison of Monte Carlo simulation results (open symbols) and experimental measurements (solid symbols) of the crystal azimuth dependence of the projectile K Auger yields for 60-keV N^{6+} ions incident at different angles on Cu(001); electron emission direction is normal to the surface.

tion results for the crystal azimuthal dependence are smaller than the size of the data points shown.

Figure 16 gives some physical insight into the reason behind these intensity modulations. The figure compares simulated K Auger spectra at 20°, 10°, and 5° incidence angles for two different crystal azimuths, $\phi=45°$ (i.e., along the [110] direction), and $\phi=35°$, for electron emission normal to the surface. The figure shows explicitly two distinct components comprising the simulated spectra. The first is electron emission occurring while the projectile is traveling in the target, and the second is electron emission occurring after a reflected projectile has left the surface. Note the interesting reversal of effects at the two azimuths evident in the 10° and 5° simulated spectra in comparison with the 20° spectra. For the latter incidence angle, both the subsurface and the particle reflection components increase when going to the $\phi=35°$ azimuth, indicating that the projectile trajectories in the bulk are on average more shallow than for the [110] direction. For the 10° and 5° incidence angles, on the other hand, the opposite trend is noted, in that the bulk trajectories appear to be more shallow when the beam direction is aligned with the crystal [110] direction than when it is not. Evidently, for the 20° incidence case, the scattering cone about the incident beam direction due to binary collisions with the first one or two crystal layers is such as to enhance encounters with subsequent layers when the azimuth is at 35°, while for the other two incidence angles encounters with subsequent layers are more probable when the azimuth is close to one of the low index directions. Similar azimuthal orientation effects have been previously noted [32]. Superimposed on the simulation results for 5° incidence angle are measured spectra for the two different azimuths displayed on the same absolute scale. As can be seen, the shapes of the measured and calculated energy distributions are in good agreement, and the variation in intensity when the azimuth is changed is well reproduced.

The variation in the yields over the whole range of azimuthal angles between the [100] and [110] directions, already shown in Fig. 15, is displayed on an expanded scale in Fig. 17 for the 5° incidence angle case. In view of the poorer agreement obtained for the two larger incidence angles, the good accord seen for this incidence angle may at first seem to be fortuitous. However, it should be noted that, with increasing incidence angle, the simulation's approximation to the electron transport to the surface by use of the inelastic mean free path becomes poorer as the projectile trajectories lie progressively deeper below the target surface, due to the broad source function used. When the probabilities for electron escape without inelastic scattering, calculated using the inelastic mean free path, become less than half, the characteristics of the observed electron emission are by definition dominated by inelastic scattering. It is likely that, under such conditions, our simple treatment of electron transport may be inadequate. As has already been noted, this limitation of

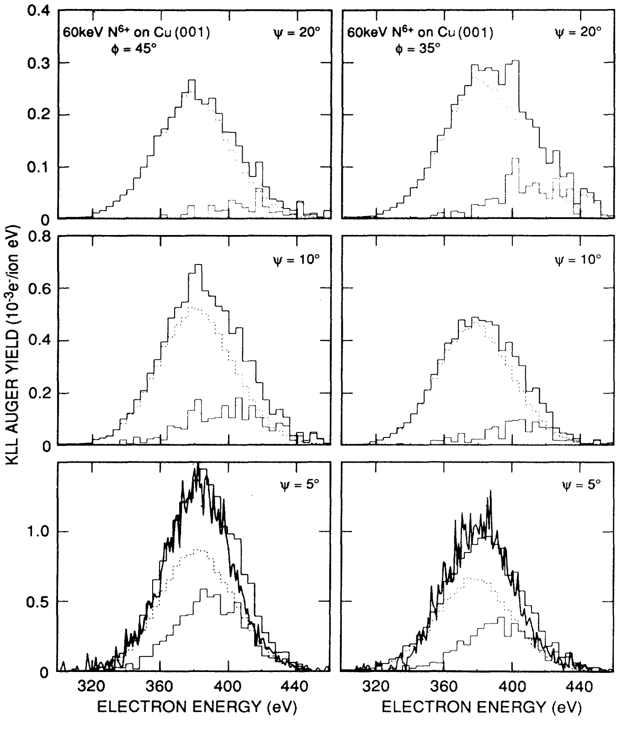

FIG. 16. Monte Carlo simulation results for the projectile K Auger line shapes (bold histrogram) at two different Cu crystal azimuths as a function of incidence angle for electron emission normal to the surface. Dashed histrogram—contribution due to subsurface emission; thin line histogram—contribution due to particle reflection (see text). For the 5° incidence case, the corresponding experimental spectra are shown, plotted on the same absolute scale.

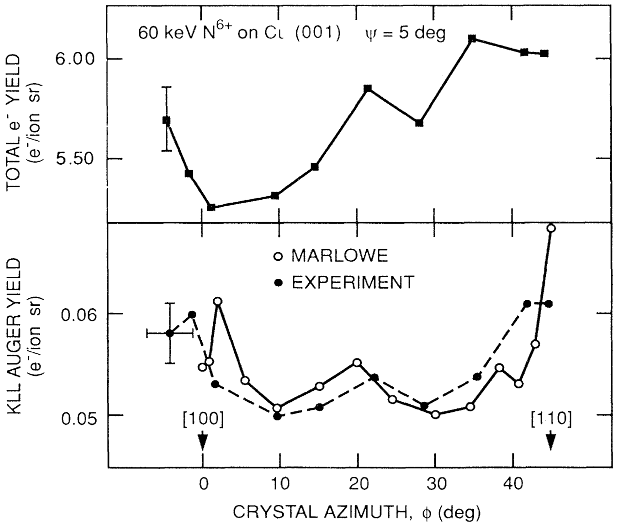

FIG. 17. Comparison of simulated and measured Cu crystal azimuth dependence of projectile K Auger electron yields for 5° incidence angle observed normal to the surface. Also shown is azimuth dependence of total measured electron yields for the same observation direction.

the simulation may also be at least partially responsible for the progressively poorer agreement between the measured total yields and the simulated yields as the incidence angle increases above 10° (see Figs. 9 and 10). For completeness, Fig. 17 also shows the azimuthal dependence of the total (i.e., energy integrated) observed electron yields. As can be seen, the azimuthal variation of the total electron yields is quite similar to that of the *K* Auger yields. We did not observe a similar correlation for the 20° angle of incidence case, where total yields were also measured as a function of crystal azimuth.

VIII. ABOVE-SURFACE NEUTRALIZATION

The discussion so far has focused on processes occurring after the projectile penetrates the target surface. We amplify in this final section our earlier discussion [9] of the possibility that, at the extreme grazing angles, neutralization processes above the surface may also become significant. The evidence for this possibility based on an analysis of electron spectra measured for the Au(110) target has been presented in a previous paper.

Briefly, the focus of the analysis in that paper was on the evolution of the shape of the projectile *K* Auger peak as a function of incidence angle. This evolution is shown in Fig. 18, where the *K* Auger peak for each incidence angle has been scaled to have the same height (note scale factors to the left of each peak). As can be seen, the spectral shapes of the peaks remain virtually unchanged as the incidence angle is increased above 4.5°. For angles less than 4.5°, however, a small feature (highlighted in black in Fig. 18) is seen to appear on the low-energy slope of the main peak, which is most prominent in the 0.5° spectrum. The presence of this lower-energy component in the overall *K* Auger peak shape is more apparent in Fig. 18b, where the main peak represented by the shape of one of the large angle spectra has been subtracted. A similar evolution of the projectile *K* Auger peak shape is observed in the case of the Cu(001) target, as can be seen in Fig. 19. The poorer statistics evident in Fig. 19 stem from the fact that, for this series of measurements, the einzel lens in front of the electron spectrometer was not used, resulting in about a factor 3 lower signal rate due to the smaller collection solid angle in that case. This was of course taken into account in the determination of the absolute intensity scale.

The main component of the projectile *K* Auger peaks evident in both figures is ascribed to subsurface electron emission, already discussed earlier. We ascribe the smaller component that becomes evident at incidence angles below about 1.6° for both targets, to above-surface neutralization via the deexcitation cascade of the Arifov model mentioned earlier. Figures 9 and 10 show experimentally determined integrated intensities of this lower-energy component, as well as two different calculations of the above-surface neutralization contribution to the observed *K* Auger yields.

The first calculation is based on a numerical simulation of the above-surface autoionization cascade that has been previously described [6,9]. Briefly, the model assumes instantaneous resonant neutralization (i.e., capture of six electrons) of the projectile $n=7$ shell at a specified critical distance above the surface. This multiexcited, neutralized projectile is then allowed to deexcite by single autoionization steps (with atomic rates calculated using the Cowan Hartree-Fock code [13]) while maintaining neutrality by additional electron capture into $n=7$. The upper and lower limits bounding the results of this simulation correspond to two different assumed critical distances (40 and 20 a.u., respectively) above the surface at which classical overbarrier transitions become possible. The smaller critical distance was obtained by proper ac-

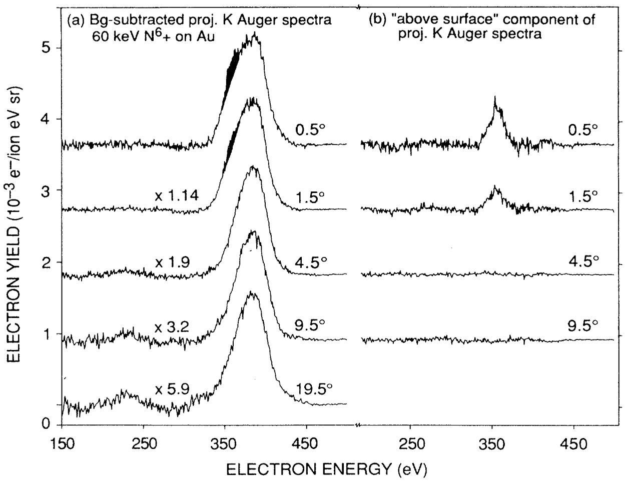

FIG. 18. (a) Background-subtracted projectile *K* Auger spectra observed for the Au target, scaled to the peak intensity of the 0.5° spectrum (note scale factors to the left of each peak). (b) Unscaled above-surface components of the *K* Auger electron spectra.

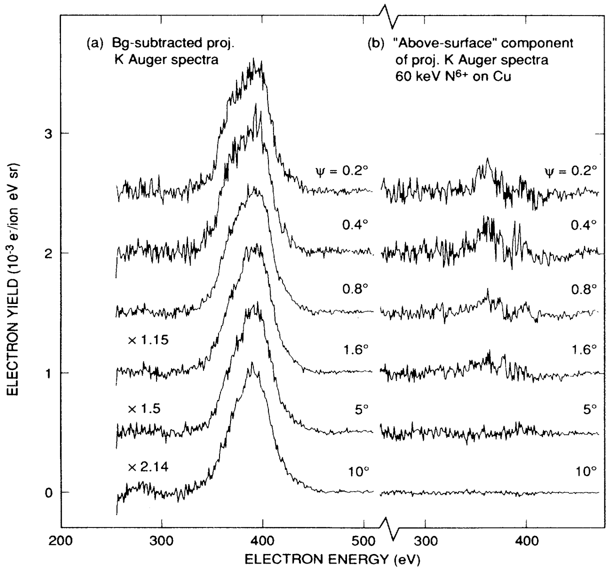

FIG. 19. Same as Fig. 18, but for the Cu target.

counting of the image potential. In the above model, use of the larger value is equivalent to doubling all the autoionization rates in the cascade, which should take into account, at least partially, possible underestimation of the rates used in the calculations, as well as the possible neglect of additional decay channels.

The second calculation [33] of the above-surface neutralization component combines a more rigorous and self-consistent treatment of the resonance neutralization process with an autoionization cascade that includes additional decay channels, and thus eliminates many of the simplifying approximations inherent in the earlier calculation. In the second calculation, the resonance neutralization is explicitly time dependent, and treated within the framework of a classical over barrier model that allows for multiple electron capture as well as loss. The effective neutralization rate and the projectile effective charge (i.e., screening effects) are calculated dynamically and self-consistently. The calculation explicitly includes the effect of the dynamical image potential both on the projectile energy levels as well as on the projectile trajectories. The image-potential-acceleration of the projectile is thus accounted for in this calculation, which was not the case for our earlier more approximate treatment. The indicated band of results for the latter model represents a large number of calculations, assuming different forms of the image potentials, the screening functions, as well as different choices of the Auger rates (see Ref. [33] for additional details).

The experimentally obtained estimates of the above-surface *K* Auger yield components for Au are in reasonable agreement with both calculations. However, for the Cu target, where the range of investigated incidence angles extends to more grazing angles, the agreement with the more comprehensive second calculation is significantly better, illustrating the importance of image potential acceleration effects on the projectile trajectories, and consequently on the time available for above-surface neutralization. In view of the good agreement with the calculated trend as a function of inverse perpendicular velocity, the premature saturation observed in the experimentally determined above-surface *K* Auger yields would suggest that image potential acceleration imposes a limit on the maximum interaction time that is available to a multicharged ion above a metal surface that is independent of its initial kinetic energy or angle of incidence. This intrinsic limit most likely makes the range of interaction times needed to make the above-surface contribution to the observed *K* Auger yields the dominant one physically inaccessible, at least for metal surfaces. It would be interesting to explore this effect further using semiconductors and insulators as targets.

In contrast to the subsurface *K* Auger emission, which occurs subsequently to almost complete *L*-shell filling, both calculations of the autoionization cascade predict close to the minimum population of the *L* shell at the time of the *K* Auger decay, implying lower *K* Auger electron energies than those characterizing the subsurface emission. This displacement is in fact evident in our measurements, where a shift of about 25 eV is noted in the above-surface components observed for both the Au and Cu targets. The peak positions of the above-surface components imply [13] *L*-shell populations of 2–3, if it is assumed that the remaining electrons are distributed in the *M* and higher shells. Similar differences in *L*-shell populations have been noted [34,35] for above- versus subsurface $K\alpha$ x-ray emission during multicharged ion surface interactions.

It could be argued that the "above-surface" components may equally well arise from reflected projectiles that have been incompletely neutralized. However, if the neutralization rate is indeed different by a factor of 5 in Au and Cu, as the comparison of our experimental and subsurface simulation results seems to indicate, it appears difficult to explain the roughly similar thresholds and magnitudes for the "above-surface" components experimentally determined for the two targets. In addition, one would not in that case expect the appearance of a discrete feature of fixed energy, but rather a more gradual broadening of the *K* Auger peak toward lower energies. Also, we measured in an auxiliary experiment the reflected ion charge state distribution for 10-keV N^{6+} ions incident on Cu at 1° and 2°. Only singly and doubly charged ions were observed (with very low intensities), indicating that, for the experimental conditions investigated, *K* Auger emission from only partially neutralized reflected projectiles is not significant.

IX. SUMMARY

We have presented in this paper measurements of *K* Auger electron emission observed during interactions of N^{6+} ions incident on Au and Cu surfaces. Results of model calculations based on a Monte Carlo simulation of the projectile trajectories inside the target were able to reproduce all the general trends manifested in the experimental results, i.e., as a function of incidence angle, observation angle, and crystal orientation. At the larger incidence angles, some of the more detailed features of the experimentally observed trends were not as satisfactorily reproduced. This small but growing divergence was attributed mainly to the approximate treatment of electron transport used in the model, which becomes inadequate when the probability for inelastic electron collisions becomes significant. Experimental problems were also noted for these larger incidence angles, such as reliable background stripping in determining the Auger yields. It is noted that all the simulation results were obtained assuming a *time-independent* interatomic scattering potential and rate of *L*-shell filling. Specifically, the potential and R_L were assumed to be independent of the degree of projectile neutralization, and the potential was not adjusted for the presence of the *K*-shell vacancy. Studies are presently underway to determine the possible limitations inherent in this approach.

At the smallest incidence angles, we observe an additional component in the *K* Auger spectra for both Au and Cu targets, which we ascribe to above-surface neutralization processes. The above-surface components are compared to two different calculations, which both indicate that for inverse perpendicular velocities above about 100 a.u.$^{-1}$, the above-surface contribution to *K* Auger emission becomes important, in qualitative agreement with the experimental results. The more sophisticated of the two calculations shows the same premature saturation of the yields as is observed experimentally for Cu at the most grazing incidence angle. This saturation is ascribed to the effect of the image potential acceleration on the projectile trajectory, which limits the interaction time available to the multicharged ion above the surface.

ACKNOWLEDGMENTS

We gratefully acknowledge the advice and help of M. T. Robinson in performing the Monte Carlo simulations. This research was supported by the Division of Chemical Sciences, Office of Basic Energy Sciences of the U.S. Department of Energy, under Contract No. De-AC05-84OR21400 with Martin Marietta Energy Systems, Inc., and by the National Science Foundation.

---

[1] S. T. de Zwart, Ph.D. thesis, University of Groningen (1987); S. T. de Zwart, A. G. Drentje, A. L. Boers, and R. Morgenstern, Surf. Sci. **217**, 298 (1989).

[2] F. W. Meyer, C. C. Havener, K. J. Snowdon, S. H. Overbury, D. M. Zehner, and W. Heiland, Phys. Rev. A **35**, 3176 (1987); F. W. Meyer, C. C. Havener, S. H. Overbury, K. J. Reed, K. J. Snowdon, and D. M. Zehner, J. Phys. (Paris) Colloq. **50**, C1-263 (1989); C. C. Havener, K. J. Reed, K. J. Snowdon, N. Stolterfoht, D. M. Zehner, and F. W. Meyer, Surf. Sci. **216**, L357 (1989).

[3] M. Delaunay, M. Fehringer, R. Geller, P. Varga, and H. Winter, Europhys. Lett. **4**, 377 (1987); M. Delaunay, R. Geller, J. Debernardi, P. Ludwig, and P. Sortais, Surf. Sci. **198**, L273 (1988).

[4] K. J. Snowdon, C. C. Havener, F. W. Meyer, S. H. Overbury, and D. M. Zehner, Phys. Rev. A **38**, 2294 (1988).

[5] L. Folkerts and R. Morgenstern, Europhys. Lett. **13**, 377 (1990); J. Phys. (Paris) Colloq. **50**, C1-541 (1989).

[6] P. A. Zeijlmans van Emmichoven, C. C. Havener, and F. W . Meyer, Phys. Rev. A **43**, 1405 (1991).

[7] H. J. Andrä, A. Simionovici, T. Lamy, A. Brenac, G. Lamboley, J. J. Bonnet, A. Fleury, M. Bonnefoy, M. Chassevent, and S. Andriamonje, Z. Phys. D (to be published).

[8] H. J. Andrä, Nucl. Instrum. Methods B **43**, 306 (1989).

[9] F. W. Meyer, S. H. Overbury, C. C. Havener, P. A. Zeijlmans van Emmichoven, and D. M. Zehner, Phys. Rev. Lett. **67**, 723 (1991).

[10] *Microchannel Plate Report,* edited by H. Kersten, Technische Informatie Post, Instituut voor Atoom en Moleculfysica, Amsterdam-Watergraafsmeer, Chap. 1.

[11] H. Kudo, D. Schneider, E. P. Kanter, P. W. Arcuni, and E. A. Johnson, Phys. Rev. B **9**, 4899 (1984).

[12] L. H. Toburen, W. E. Wilson, and H. G. Paretzke, Phys. Rev. A **25**, 713 (1982).

[13] R. D. Cowan, *The Theory of Atomic Structure and Spectra* (University of California Press, Berkeley, 1981).

[14] D. A. Shirley, Phys. Rev. B **5**, 4709 (1972).

[15] H. E. Bishop, Surf. Interface Anal. **3**, 272 (1981).

[16] M. T. Robinson, Phys. Rev. B **40**, 10 717 (1989).

[17] For example, J. F. Ziegler, J. P. Biersack, and U. Littmark, in Proceedings of the U.S.-Japan Seminar on Charged Particle Penetration Phenomena, January, 1982, Honolulu, Hawaii, [ORNL Report No. CONF-820131, 1983, (unpublished)].

[18] S. H. Overbury *et al.*, in Proceedings of the International Conference on Atomic Collisions in Solids, Salford, U.K., July 1991 [Nucl. Instrum. Methods B (to be published)].

[19] M. P. Seah and W. A. Dench, Surf. Interface Anal. **1**, 1 (1979).

[20] M. O. Krause, J. Phys. Chem. Ref. Data **8**, 307 (1979).

[21] Since $R_L \gg R_K$ for the Cu target, the yield dependence on incidence angle is approximately described by a single time constant $\sim 1/R_k = 10^{-14}$ s, similar to the finding of L. Folkerts and R. Morgenstern [Z. Phys. D (to be published)], who obtained $\tau_{KLL} = 4.6 \times 10^{-15}$s for O^{7+} incident on W.

[22] Jörg Müller and Joachim Burgdörfer, Phys. Rev. A **43**, 6027 (1991).

[23] F. J. Rogers, H. C. Graboske, and D. J. Harwood, Phys. Rev. A **1**, 1577 (1970).

[24] T. L. Ferrell and R. H. Ritchie, Phys. Rev. B **16**, 115 (1977).

[25] P. M. Echenique, R. M. Nieminen, J. C. Ashley, and R. H. Ritchie, Phys. Rev. A **33**, 897 (1986); P. M. Echenique, F. Flores, and R. H. Ritchie, in *Solid State Physics: Advances in Research and Applications,* edited by H. Ehrenreich and D. Turnbull (Academic, New York, 1990), Vol. 43, p. 229.

[26] For example, E. Umbach, J. C. Fuggle, and D. Menzel, J. Electron, Spectrosc. Relat. Phenom. **10**, 15 (1977). The screening effect due to conduction electrons is manifested as a shift of the Auger transitions to slightly higher energies, also observed in comparing gas phase Ar *LMM* Auger transitions with those for Ar implanted in Be and Si [D. M. Zehner and H. H. Madden, J. Vac. Sci. Technol. **16**, 562 (1979)]. The same shift of about 7.5 eV is seen in the Ar *LMM* spectra measured by de Zwart for Ar^{9+} projectiles incident on a W metal target (Ref. [1]).

[27] R. H. Ritchie (private communication).

[28] For example, C. Kittel, *Introduction to Solid State Physics,* 4th ed. (Wiley, New York, 1971), p. 39.

[29] B. Lesiak, A. Jablonski, Z. Prussak, and P. Mrozek, Surf. Sci. **223**, 213 (1989).

[30] C. S. Fadley and D. A. Shirley, J. Res. Natl. Bur. Stand., Sect. A **74**, 543 (1970).

[31] For example, N. Stolterfoht, in *The Physics of Ionized Gases,* edited by R. K. Janev (Institute of Physics, Beograd, 1979), p. 93; in *Progress in Atomic Spectroscopy,* edited by H. Kleinpoppen (Plenum, New York, 1987), Pt. D, p. 415.

[32] For example, H. J. Andrä, H. Winter, R. Fröhling, N. Kirchner, H. J. Plön, W. Wittman, W. Graser, and C. Varelas, Nucl. Instrum. Methods **170**, 527 (1979).

[33] J. Burgdörfer, P. Lerner, and F. W. Meyer, Phys. Rev. A **44**, 5674 (1991).

[34] M. Schulz, C. L. Cocke, S. Hagmann, M. Stöckli, and H. Schmidt-Böcking, Phys. Rev. A **44**, 1653 (1991).

[35] J. J. Bonnet, A. Fleury, M. Bonnefoy, M. Chassevent, T. Lamy, A. Brenac, A. Simionovici, H. J. Andrae, and S. Andriasmonje, Z. Phys. D (to be published).